A Low Cost Battery-Balancing Auxiliary Power Module with Dual Active Half Bridge Links and Coreless Transformers

Weizhong Wang, Youssef A. Fahmy, *Student Member, IEEE* and Matthias Preindl, *Senior Member, IEEE*

***Abstract*—Redistributive balancing brings many benefits to electric vehicles, such as increased range and more uniform cell degradation. Despite previous analyses suggesting a 17-36% extension of battery lifetime, the cost of such systems has prevented the technology from being adopted in practice. This study proposes a simplified topology for battery-balancing auxiliary power modules with reduced magnetic material to achieve cost-friendly solutions without sacrificing functionality or balancing modes. The proposed system consists of a dual-active half bridge, halving the number of switches needed compared with the conventional dual-active bridge. In addition, the transformer core material is removed and a coreless transformer is used to provide isolation and energy transfer. Both changes reduce the cost of redistributive balancing. The topological modeling differs from cored transformer circuits as the coupling of the coreless transformer is weaker. The coupling coefficient is now used in an updated model that includes transformer currents and output powers. These, along with the balancing modes, are analyzed then experimentally verified. The proposed models can guide the selection of MOSFETs and the design of the coreless transformer. An analytic projection shows up to a 22% cost reduction compared with similar topologies.**

***Index Terms*—Auxiliary power module, battery balancing, battery aging, coreless transformer, DC/DC converter, dual half bridge, electromagnetic design**

I. Introduction

THE attention given to electrical vehicles (EVs) has escalated as they have emerged as a promising alternative to fossil fueled, internal combustion vehicles. Their charging stations can use domestically generated energy from renewable resources, such as wind or solar. However, range anxiety and battery aging have been major concerns for end users, leading to slower adoption.

The battery cells in a series- and parallel-connected pack share non-uniformly distributed loads and can degrade irregularly because of both internal and external stresses. Impedance and capacity differences introduced by manufacturing tolerances [1] or temperature variation based on the locations of the cells [2], [3] are examples of systemic differences. As a result, performance and driving range will be compromised.

Battery balancing techniques as a means of mitigating the aforementioned concerns have been intensively studied. The two major balancing strategies are dissipative and redistributive balancing. Dissipative balancing involves any mechanisms that reject excess energy, e.g. gas leaking for Lead-acid batteries [4] and shunt resistor dissipation (active or passive) for Lithium Ion batteries [2], [3], [5].

W. Wang, Y.A. Fahmy and M. Preindl are with the Department of Electrical Engineering, 500 W. 120th St., Mudd 1310, New York, NY, USA 10027 (e-mail: ww2427@columbia.edu; y.fahmy@columbia.edu*; matthias.preindl@columbia.edu)

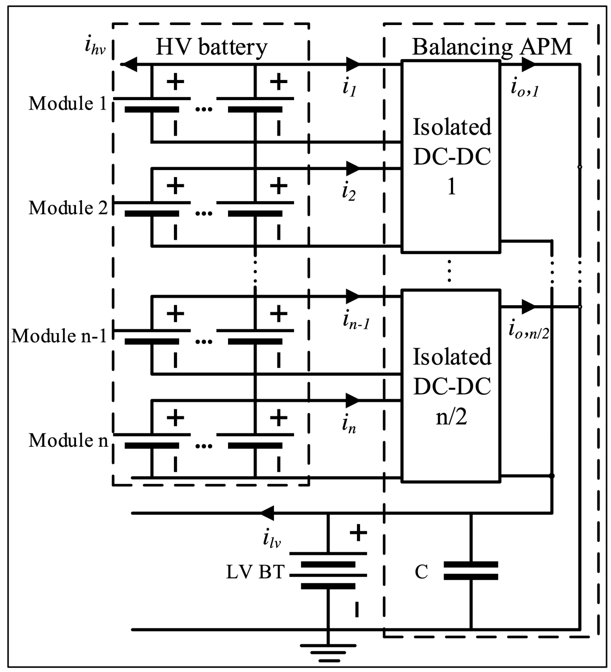

Fig. 1: Pack level layout of dual-active half bridge (DAHB) converters serving both the high and low voltage batteries

Redistributive balancing shuttles excess energy from 'strong' to 'weak' cells using energy storage components such as switched-capacitive [6], [7], switched-inductive [4], [8]–[10], and individual power converters [2], [11]–[15]. The switched-capacitive and -inductive configurations take longer to distribute energy in a large battery pack and are sensitive to how imbalances are resolved [2], [5]. On the other hand, converter-based redistributive balancing overcomes the aforementioned disadvantages of the switched-capacitive/inductive strategies by simultaneously managing small groups of cells on a module by module basis [2], [11]–[14].

However, installing dedicated DC/DC converters on each cell puts financial burdens on the cost of the entire battery management system (BMS). Therefore, there are many studies investigating the reduction of costs associated with the power electronic components. A battery-balancing auxiliary power module (BB-APM) is a concept that integrates battery balancing in the auxiliary power module (APM), such that the feasibility of implementing redistributive balancing in practice can be justified [2], [11], [16]. The system structure showing the interface between the high and low voltage systems is

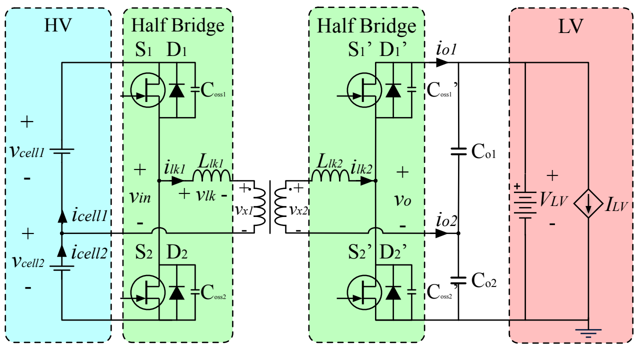

Fig. 2: DAHB DC/DC converter topology for battery-balancing auxiliary power modules

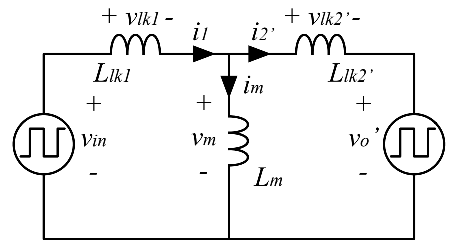

Fig. 3: The equivalent circuit model for a half-bridge air-core configuration.

shown in Fig. 1. A topological improvement compared with [11] that reduces the cost of BB-APM has been achieved in previous work [2]. This is done by reducing the number of active switches from eight per cell in a dual-active bridge (DAB) to three per cell in a half-full bridge (HFB). The BB-APM now also achieves an extra cell-to-cell (C2C) balancing mode.

Other converters, such as those reviewed in [17] do not incorporate low voltage distribution. The advantage of reducing both the weight and volume by incorporating the low voltage interface, while maintaining cell to cell balancing at a reduced cost, is key to the contributions of this technology. Furthermore, [18] has an approach with a similar switch-to-cell ratio as presented here but crucially does not include auxiliary power capabilities. This means an entirely separate device will be needed to keep the low voltage battery charged, adding weight and cost.

To further reduce costs, this paper proposes further modifications to the BB-APM topology of [2] by utilizing a DAHB [19] and integrating the previously discrete inductor into a coreless transformer, which is shown in Fig. 2. The number of active switches per cell is reduced to two compared to three in [2] and eight in [11]. In addition, the expensive ferromagnetic core is eliminated. The modifications proposed in this study reduce the costs of the MOSFETs and magnetic materials by 33% and 100%, respectively, while still providing all of the balancing modes of [2]. The modifications, particularly the removal of the core, necessitate new analysis.

This paper is organized as follows, the system model involving the coreless transformer is derived in Section II. The transient and steady-state root mean squared (RMS) currents of the transformer and output power models are given in Section III. Utilizing the derived system models, design criteria are explained in Section IV. A prototype is developed and validated in Section V. Lastly, the paper is concluded in Section VI.

II. System Model Considering Loosely Coupled Coreless Transformer

Conventional DAB and DAHB designs utilize either discrete inductors or leakage inductors introduced by the transformers [2], [11], [19], [20]. In the latter designs, the current flowing through the magnetization inductor can be ignored since it is significantly larger than the leakage inductance. Therefore, the system model is normally derived assuming that the magnetization inductor is open-circuited [20], [21], which reduces derivation complexity. However, coreless transformers have a higher leakage inductance even when the primary and secondary windings are placed close together [18], [22]. Thus the leakage inductance becomes comparable with the magnetization inductance and the current flowing through each becomes comparable, changing the expressions of currents and power. Potential efficiency losses can be mitigated by switching to a variable frequency scheme as in [23]. A simplified equivalent circuit model (ECM) of the DAHB is illustrated in Fig. 3 for the case where the magnetization inductance cannot be treated as an open circuit.

Applying KCL and KVL on the ECM gives

$$i_1 = i_m + i_2' \tag{1}$$

$$V_{in} - v_m(t) = L_{lk1}\frac{di_1(t)}{dt} \tag{2}$$

$$v_m(t) - v_o'(t) = L_{lk2}'\frac{di_2'(t)}{dt} \tag{3}$$

$$v_m(t) = L_m\frac{di_m(t)}{dt} \tag{4}$$

where the currents $i_1(t)$, $i_2'(t)$, and i_m are the primary, primary-referred secondary, and magnetization currents. The voltage across the magnetization inductor is denoted as $v_m(t)$. The two switch-node voltages on the primary and primary-referred secondary sides are v_{in} and v_o'. The primary leakage inductance and primary-referred secondary leakage inductance are L_{lk1} and L_{lk2}', respectively. The voltage across the magnetization inductor is then calculated in (5) as

$$\begin{aligned} v_m(t) &= L_m\left(\frac{di_1(t)}{dt} - \frac{di_2'(t)}{dt}\right) \\ &= L_m\left[\frac{v_{in}(t) - v_m(t)}{L_{lk1}} - \frac{v_m(t) - v_o'(t)}{L_{lk2}'}\right] \\ &= \frac{L_{lk1}v_o'(t) + L_{lk2}'v_{in}(t)}{\frac{L_{lk1}L_{lk2}'}{L_m} + L_{lk1} + L_{lk2}'}. \end{aligned} \tag{5}$$

It can be seen that the magnetization voltage is dependent on the leakage inductances and the ratio of L_{lk1} and L_m, which is in turn dependent on the coupling of the transformer.

The main difference between cored and coreless transformers is the coupling between the windings. A tightly coupled transformer using magnetic material has most of its flux coupled between windings. This leads to a significantly

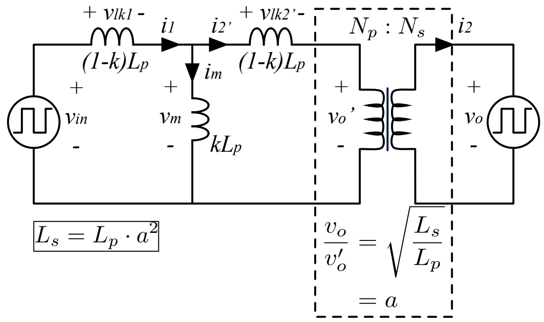

Fig. 4: The equivalent transformer model considering the coupling coefficient and nonideality

smaller leakage inductance than magnetization inductance. If the windings are not placed sufficiently close when the ferric core is removed, a high amount of flux traverses only through its own winding instead of linking with others. The coupling coefficient is commonly used to quantify the extent of the coupling between the windings and is defined as

$$k = \frac{L_m}{L_{self}} = \frac{L_m}{L_m + L_{lk}}, \tag{6}$$

where L_{self} is the self inductance, a sum of magnetization inductance L_m and leakage inductance L_{lk} referred to either side. The higher the coupling, the smaller the magnetizing currents that are induced, resulting in lower loss.

Depending on transformer configuration, the switch node voltage varies, which changes the leakage current and circuit operation. Therefore, the voltages across the leakage inductors will be analyzed first based on transformer configurations.

1) Leakage Inductor Voltage of Cored Transformers: With cored transformers, the coupling coefficient can be as high as 0.999, which translates to a ratio of leakage and magnetization inductance of 1000. Therefore, the term $\frac{L_{lk1}L_{lk2}}{L_m}$ in (5) can be neglected without noticeable error. The magnetization voltage can then be simplified using $L_{lk1} = L'_{lk2}$ to

$$v_m = \frac{v_{in}(t) + v'_o(t)}{2} \tag{7}$$

which determines the primary leakage inductor voltage as

$$v_{lk1}(t) = v_{in}(t) - v_m(t) = \frac{v_{in}(t) - v'_o(t)}{2}. \tag{8}$$

This equation shows that the voltage across the primary leakage inductor is no longer $v_{in}(t) - v'_o(t)$ because half is now applied to the leakage inductor. As a result, the rate of current change, and therefore the output power, is halved for the same switching frequency as the discrete inductor topology.

2) Leakage inductor voltage of coreless transformer: When the core is removed, the term $\frac{L_{lk1}L'_{lk2}}{L_m}$ in (5) cannot be ignored anymore as the flux regulation is significantly worse. This leads to a leakage inductance that is comparable to the magnetization inductance. Consequently, $v_m(t)$ will be less than what is derived in (8) and will be related to the coupling coefficient, which then complicates the entire circuit design. To better illustrate the change, the equivalent transformer model considering coupling coefficient k and primary self inductance L_p is given in Fig. 4. It shows a transformer with a physical turns ratio of $N_p : N_s = 1 : n$ and coupling coefficient $k \subset [0, 1]$. However, the relationship mapping the secondary value to the primary side is not necessarily equal to the physical turns ratio [24]. A coreless transformer is equivalent to an ideal transformer with a turns ratio of

$$N_p : N_s = 1 : \sqrt{L_s/L_p} = 1 : \sqrt{L_{lk2}/L_{lk1}} = 1 : a, (a \leq n). \tag{9}$$

The primary self inductance and secondary self inductance are denoted as L_p and L_s, respectively. All primary-referred secondary parameters need to be converted using the new effective turns ratio *a* rather than the physical turns ratio *n*. The magnetization inductance is represented by $L_m = kL_p$. Due to imperfect coupling, the flux not linked with the opposite winding creates the leakage inductance that is related to k.

The leakage inductances L_{lk1} and L_{lk2} can also be expressed as $(1-k)L_p$ and $(1-k)L_s$, respectively. Referred to the primary, the leakage inductance L'_{lk2} equals to L_{lk1}. The term $\frac{L_{lk1}L'_{lk2}}{L_m}$ can be therefore simplified to $\frac{1-k}{k}L_{lk1}$ and

$$v_m = \frac{v'_o(t) + v_{in}(t)}{\frac{1-k}{k} + 2} \overset{K=\frac{1-k}{k}}{=} \frac{v'_o(t) + v_{in}(t)}{K + 2}, \tag{10}$$

$$v_{lk1} = \frac{v_{in}(t) - \frac{v'_o(t)}{K+1}}{1 + \frac{1}{K+1}}, \tag{11}$$

$$v_{lk2} = v_m - v'_o(t) = \frac{\frac{v_{in}(t)}{K+1} - v'_o(t)}{1 + \frac{1}{K+1}}. \tag{12}$$

Equations (10) - (12) determine the shape of the magnetization, primary leakage, and secondary leakage current waveforms. Applying a phase angle d for phase shift control [2] between the primary and secondary switches enables power flow from one side to the other. In addition, a small duty cycle adjustment, θ, on the primary switches is introduced to maintain a volt-amp (VA) balance on the transformer and to adjust the direct current (DC) current flowing through the transformer [2]. The primary switch S_1 is turned on for $50\% - \theta$ of one period whereas the switch S_2 conducts for a complimentary $50\% + \theta$ of one period. The duty cycle adjustment has been previously explained and calculated in [2] and is adopted here as

$$\theta = \frac{T}{2}\left(\frac{V_{cell1} - V_{cell2}}{V_{cell1} + V_{cell2}}\right) = \frac{T}{2}\frac{V_\Delta}{V_\Sigma}, \tag{13}$$

where the switching period is denoted as T. Assuming the switching is sufficiently fast and the voltages are stabilized by the filtering capacitors, the cell voltages v_{cell1} and v_{cell2} can be approximated by their constant voltages V_{cell1} and V_{cell2}, respectively. V_Σ is the sum of the two cell voltages while the difference of the two cell voltages is represented by V_Δ. By properly controlling the duty cycle adjustment, the DC current of the transformer can be regulated, resulting in arbitrary cell currents. Therefore, various levels of C2C balancing can be achieved.

The switching sequence and the control method for applying phase shift and duty cycle adjustments within a switching period are given in Table I. Combining (10) - (12) and Table I

TABLE I: Switching sequence with phase shift and duty cycle adjustment during a switching period T

Time slot	Switch				$v_{in}(t)$	$v_o(t)$
	S_1	S_2	S_1'	S_2'		
0 - d	On	Off	Off	On	v_{cell1}	v_{co2}
d - $0.5T-\theta$	On	Off	On	Off	v_{cell1}	v_{co1}
$0.5T-\theta$ - $d+0.5T$	Off	On	On	Off	v_{cell2}	v_{co1}
$d+0.5T$ - T	Off	On	Off	On	v_{cell2}	v_{co2}

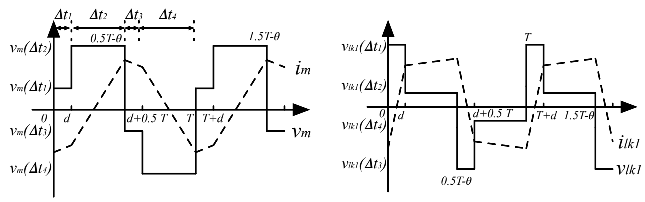

(a) (b)

Fig. 5: The waveforms of (a) magnetizing inductor and (b) primary leakage inductor, a similar waveform exists for the primary-referred secondary leakage

results in the magnetizing and leakage inductor currents shown in fig. 5.

III. RMS CURRENTS AND OUTPUT POWER

MOSFET selection and transformer design are mainly determined by the RMS current flowing through the device and the rated output power requirements. The RMS currents govern the conduction losses in the transformer and the MOSFETs. The transformer design, i.e., the leakage inductance and turns ratio in the conventional DAB or DAHB designs, combined with the switching frequency sets an absolute boundary on the output power capability regardless of phase shift [2], [25], [26]. However, the previously derived RMS and output power models in other literature are not valid for coreless transformers due to imperfect coupling. Therefore, it is worthwhile to develop RMS and power models for the proposed topology.

A. RMS currents

In combination with (11) and (12), the RMS current on the primary leakage inductor inductor is obtained from a piecewise analysis of the waveform shown in Fig. 5b. The equation is shown in (14) and a similar derivation is undertaken for the primary-referred secondary leakage in (15). These will be utilized to define the maximum RMS current along with the model of the output power.

B. Output Power

In the DAHB configuration, the existence of two capacitors on the output means the output power consists of power on both the high-side capacitor C_{o1} and low-side capacitor C_{o2} i.e., $p_o(t) = p_{o1}(t) + p_{o2}(t)$. Assuming the two capacitor voltages are balanced and remain constant during one switching period, the instantaneous power can be expressed using

$$p_o(t) = V'_{co1} i'_{o1}(t) + V'_{co2} i'_{o2}(t) = \frac{V'_{LV}}{2}\left(i'_{o1}(t) + i'_{o2}(t)\right). \tag{17}$$

The regulated output currents i'_{o1} and i'_{o2} are illustrated in Fig. 6. Based on the waveforms, the average output power is then obtained as

$$P_o(t) = \frac{V'_{LV}}{2}\frac{1}{T}\int_d^{T+d} (i'_{o1}(t) + i'_{o2}(t))dt. \tag{18}$$

1) Transient output power: The initial conditions $i'_{o1}(d)$ and $i'_{o2}(d)$ are needed to perform the integral in (18). It can be seen from Fig. 6 that

$$i'_{o1}(d) = i'_{o2}(d) = i'_{lk2}(d) = i'_{lk2}(0) + \frac{v'_{lk2}}{L'_{lk2}} d \tag{19}$$

where, considering the average current of i'_{lk2} to be zero, the initial current $i'_{lk2}(0)$ can be calculated as follows:

$$I'_{lk2} = \frac{1}{T}\int_0^T i'_{lk2}(t)dt = 0 \tag{20}$$

$$i'_{lk2}(0) = \frac{k\left[V_1\alpha_{lk2,i_0} + V_2\beta_{lk2,i_0} + 2V'_o(1-2d')\right]}{8fL'_{lk2}(k+1)} \tag{21}$$

where

$$\begin{aligned}\alpha_{lk2,i_0} &= -3 + 2\theta' + \theta'^2\\ \beta_{lk2,i_0} &= 1 + 2\theta' + \theta'^2.\end{aligned}$$

Then the averaged output currents from each branch I'_{o1} and I'_{o2} on the secondary side can be obtained as follows:

$$I'_{o1} = I'_{o2} = \frac{k}{k+1}\frac{1}{16fL'_{lk2}}(V_1\alpha_{lk2,i_o} + V_2\beta_{lk2,i_o}) \tag{22}$$

where

$$\begin{aligned}\alpha_{lk2,i_o} &= -1 + 4d' + 2\theta' - 2d'^2 - \theta'^2 - 4d'\theta'\\ \beta_{lk2,i_o} &= 1 + 2\theta' - 2d'^2 - \theta'^2 - 4d'\theta'.\end{aligned}$$

Therefore, the total output power is then equal to

$$\begin{aligned}P_o &= (I'_{o1} + I'_{o2})\frac{V'_{LV}}{2}\\ &= \underbrace{\frac{k}{k+1}}_{\text{Reduction factor}}\frac{1}{16afL'_{lk2}}V'_{LV}(V_1\alpha_{lk2,i_o} + V_2\beta_{lk2,i_o}),\end{aligned} \tag{23}$$

which is consistent with the design of cored transformers when $k \to 1$ and $a \to n$.

This equation states that there is a power reduction due to the imperfect coupling of a coreless transformer. It shows that if the coupling is as low as 0.7, the output power drops to 80% of the power of the DAHB that uses tightly coupled transformers with cores. Should a drop-in air-core replacement design for a cored transformer be desired without modifying the circuit, it can be achieved by tuning the operating frequency. The power reduction due to the lowered coupling coefficient can then be compensated for by decreasing operating frequency. However, the maximum RMS current stress of each component has to be checked against the datasheet to ensure compliance.

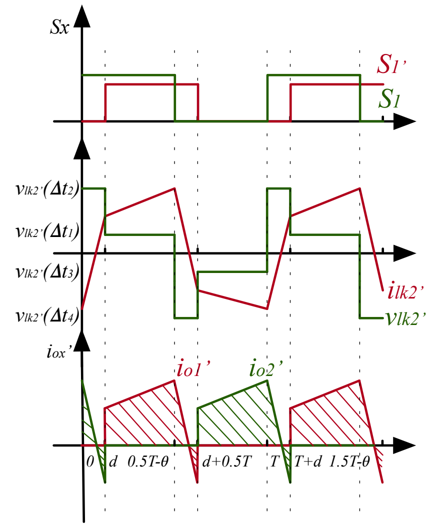

Fig. 6: The secondary leakage current and voltage based on phase shift control as well as the output currents filtered by two output capacitors

2) Steady-state output power: In both the initial conditions of (21) and in the output power of (23), the duty cycle adjustment θ can be replaced by its steady-state value of (13). This gives

$$i'_{lk2}(0) = \frac{V_o V_\Sigma - 2V_o V_\Sigma - 2akV_1V_2}{4fL'_{lk2}aV_\Sigma(k+1)}. \tag{24}$$

The steady-state initial condition can be used for steady-state output calculations as follows

$$\begin{aligned} P_o &= G_P P_{o,base} \\ G_P &= \frac{k}{k+1}\frac{1}{8a}\frac{1}{fL'_{lk2}} \\ P_{o,base} &= V_{LV}\left(-V_\Sigma d'^2 + 2V_2 d' + \frac{V_2V_\Sigma - 2V_2^2}{V_\Sigma}\right), \end{aligned} \tag{25}$$

where the output power is divided into the transformer-independent factor, $P_{o,base}$, and the transformer-dependent factor, G_P . The transformer-independent component is a function of the operating range determined by the particular BB-APM application, e.g. cell 1 and 2 voltage range and phase shift, rather than the specific transformer design. The factor $P_{o,base}$ is a typical quadratic function of d' with a maximum located at $d' = \frac{1}{V_1/V_2+1}$ and can be pre-calculated for a defined application. On the other hand, the multiplier G_P is based on transformer design choices and the frequency operating point.

IV. Design criteria

The previously derived system models of RMS current and output power are applied here to design a prototype that fulfills the design requirements of an APM.

A. Output power requirement

The rated power of the auxiliary power modules is determined based on the particular electric vehicle in question. The low-voltage (LV) loads vary with the installed auxiliary packages, e.g. seat heating and multimedia hubs. From a review of previous literature, it is determined that the rated power ranges between 1.2 and 2.4 kW [27]. Therefore, for a 100-cell/module HV battery system, an output power of 12-24 W between each cell/module and the LV battery should be guaranteed. As two cells are managed by one DAHB, the DAHB should be rated for 24-48 W and can be designed accordingly based on (25). In this study, the DAHB is designed to deliver up to 48 W with a rated power of 36 W. However, delivering rated power is not practical when the cells approach empty as the remaining energy should be conserved to extend the EV's driving range. Therefore, a threshold where the rated power is not required is set to be 20% of the state of charge (SOC), which translates to a cell voltage of around 3.32 V for an NMC cell [2]. It can be adjusted if a different threshold is desired. This threshold will be used later in the design process.

Prior to determining the parameters of the transformer, the minimum of the transformer-independent factor, $P_{o,base}$, can be obtained in order to find the required G_P that enables a maximum 48 W output, i.e.,

$$G_{p,required} \geq \frac{\max(P_o)}{\min(P_{o,base}|d' = 0.5)} \tag{26}$$

The factor $P_{o,base}$ is dependent on the cell voltages and the phase shift which is fixed at 0.5 for maximum power delivery at the given operating frequency. A minimum can be found by using an optimization tool or a parameter sweep. The minimum of $P_{o,base}$ is found to be located where the cell and LV voltages reach minimum. Some representative samples of power curves are shown in Fig. 7. They show that the minimum of $P_{o,base}$ is at 19.92 when the cells are at a minimum threshold of 3.32 V beyond which the system is required to provide the rated power. The desired G_P can be obtained based on (26):

$$G_{p,required} = \frac{k}{k+1}\frac{1}{8afL'_{lk2}} \geq \frac{48}{19.92} \geq 2.4. \tag{27}$$

$$I_{lk1,rms} = \frac{T}{4\sqrt{3}L_{lk1}(V_1+V_2)(k+1)}\sqrt{k^2V_o'^2(V_1+V_2)^2 + 4a^2V_1^2V_2^2 - 4akV_o'\Gamma} \tag{14}$$

$$I_{lk2,rms} = \frac{T}{4\sqrt{3}L_{lk2}a(V_1+V_2)(k+1)}\sqrt{V_o'^2(V_1+V_2)^2 + 4a^2k^2V_1^2V_2^2 - 4akV_o'\Gamma} \tag{15}$$

$$\Gamma = V_1^3d^3 + 3V_1^2V_2d^3 - 3V_1^2V_2d^2 - 3V_1^2V_2d + 3V_1V_2^2d^3 - 6V_1V_2^2d^2 + 3V_1V_2^3 + V_2^3d^3 - 3V_2^3d^2 + 3V_2^3d - V_2^3 \tag{16}$$

*Note that $V_1 = V_{cell1}$ and $V_2 = V_{cell2}$ for cleaner presentation

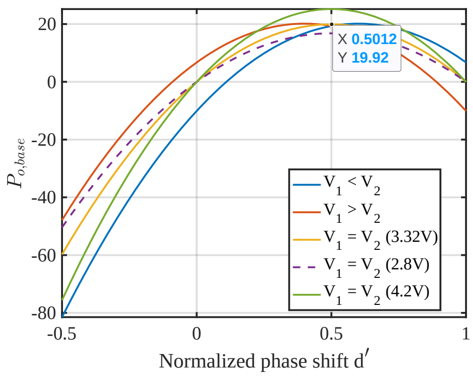

Fig. 7: $P_{o,base}$ vs phase shift d' at extreme conditions

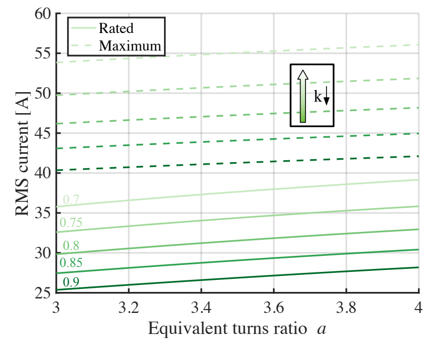

Fig. 8: The worst primary leakage RMS current with different coupling factors and effective turns ratios

As long as the transformer parameters and the operating frequency are properly designed and selected based on (27), the output power requirement can be satisfied. Note that the efficiency penalty on the actual system should be added once the system efficiency map is obtained. The operating frequency should be adjusted according to the efficiency penalty.

B. RMS current requirement

The absence of core loss leads to a dominant conduction loss. Determining the RMS currents of the primary and secondary leakage inductors help determine the conduction losses from each component, e.g. the MOSFETs and the transformer. The RMS currents can be obtained at each operating point, allowing the losses to be calculated. However, it is worthwhile to locate the operating point with the highest conduction losses, i.e., the peak RMS currents, to identify applicable MOSFETs.

Maximum RMS current can be found by optimizing (14) and (15) with constraints set by the cell voltages and power limitations by way of the phase shift d, as in

$$\min -I_{lkx,rms} \text{ such that } \begin{cases} 3.32\ V \leq V_{cell1} \leq 4.2\ V, \\ 3.32\ V \leq V_{cell2} \leq 4.2\ V, \\ 12\ V \leq V_{LV} \leq 14\ V, \\ 36\ W \leq P_o(d) \leq 48\ W. \end{cases} \tag{28}$$

Fig. 8 illustrates the maximum RMS current on the primary side with varying equivalent turns ratio a and coupling coefficient k. It shows that the primary RMS leakage current decreases with increased k but increases with increased a. Therefore, improving the coupling in the transformer can reduce the RMS current and therefore the conduction losses.

C. Transformer Design

The coreless transformer was chosen to have a physical turns ratio of 4:1 to easily fit on a four layer PCB while providing the most current at minimal loss. Nonidealities will cause the effective turns ratio to be lower. To save space and cost, a frame design was chosen in which the transformer windings are incorporated into the same PCB as the circuit. An ANSYS-Maxwell simulation was conducted to extract parameters as shown in Fig. 9.

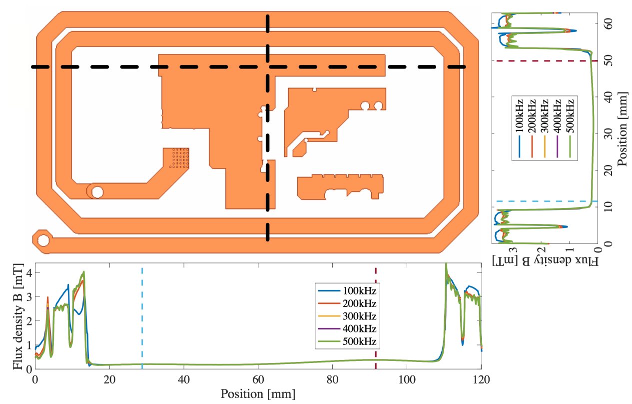

Fig. 9: Ansys Simulation of the Coreless DAHB showing the flux on one layer of the PCB

Plots of flux along the indicated axes show that the flux drops off rapidly with distance. This indicates that while the coupling is not perfect due to the absence of a core, the magnetic field will not interfere with the operation of the circuit. This phenomena was also observed for the other layers of the coreless DAHB PCB. Furthermore, the chassis of the APM will need to be grounded to reduce interference that may otherwise be radiated to other components.

V. Experimental Results

The self-designed power stage and coreless transformer are shown in Fig. 10. The parameters of the designed transformer are given in Table II. Based on the G_P requirement in (27) and the maximum RMS current in (28), the circuit needs to operate at 256 kHz or higher to provide 48 W of output power.

High fidelity Matlab-PLECS simulations were performed to design the system and verify functionality before building the full experimental setup. For example, C2C balancing was performed in Fig. 11 where one cell at a lower SoC is charged by a cell with a higher SoC, while minimal power is transferred across the inductive coupling. In the first plot, the transformer voltage is overlaid on the leakage inductor current which is almost triangular. As there is no appreciable inductive power transfer, θ, as shown in Fig. 5b is controlled to zero forming a triangular wave. Thus the power discharged from one cell is put into the other, minus any losses.

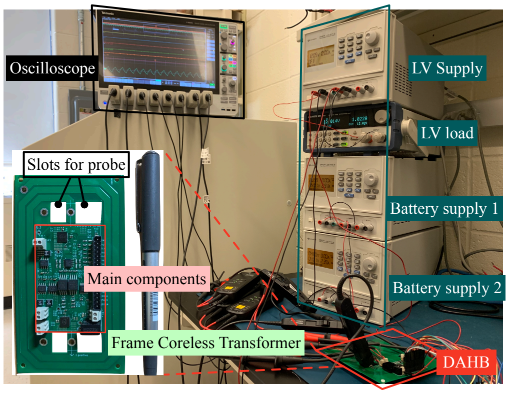

Fig. 10: The prototype of the proposed DAHB with a coreless transformer during testing.

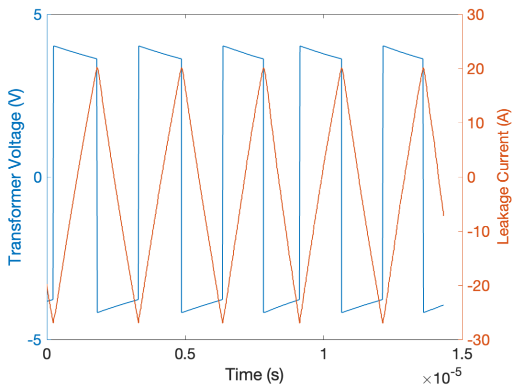

(a)

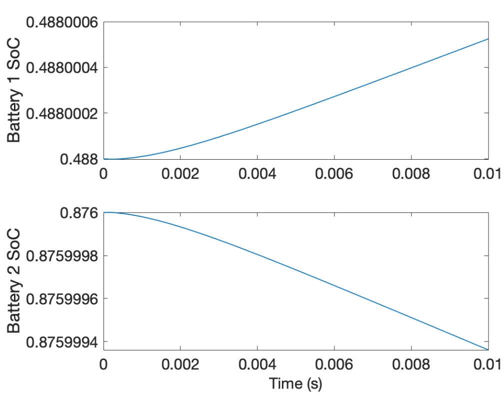

(b)

Fig. 11: Simulations of (a) transformer voltage and corresponding leakage current for C2C balancing and (b) SoCs of two cells at 4A each, they would take approximately 4 hours to fully balance

The compact half bridge SiC789 modules from Vishay are used in the power conversion stage, which is selected based on Fig. 8. To demonstrate capability, the primary cells are simulated by two DC power supplies; the LV battery and load are replaced by a DC power supply in parallel with a DC electric load. Different balancing modes have been verified on the testbench and are plotted in Fig. 12. The Cell-to-LV (C2LV) only mode where two cells provide the same amount of power to the LV load is shown in Fig. 12a. With the duty cycle adjustment θ, a DC bias can be introduced between cell currents, resulting in one cell providing more power than the other.

Cell 2 can also be entirely disabled by controlling the DC bias while doubling cell 1 current, as shown in Fig. 12c. Note that cell 2 can be set to receive charge from cell 1 if I_{DC} continues to increase. In addition, reverse power flow (LV-to-cell (LV2C)) can be achieved by reversing the phase shift angle between primary and secondary switches.

The efficiency of the prototype across the entire power range has been plotted in Fig. 13. The peak efficiency of 80% is reached at higher operating frequencies where less RMS current is flowing and the circuit is running under ZVS. Note that higher efficiency can be achieved with MOSFETs that have lower $R_{ds,on}$ and better switching characteristics at a modest cost impact, e.g. SiC, or GaN MOSFETs. Even discrete Si MOSFETs will introduce an increase in efficiency. This prototype, using the Vishay modules, focuses on demonstrating the functionality of the BB-APM using a DAHB and a coreless transformer.

The proposed topology is compared with other converter-based battery balancing topologies in Table III. It can be seen that the proposed configuration significantly reduces the number of cost-ineffective components while providing the most balancing modes. To highlight the cost improvements that stem from changing from an HFB to a coreless transformer DAHB, a cost estimation is conducted and compared with commercially available battery balancing solutions, as shown in Fig. 14. This cost comparison includes sensing circuitry, passive components, MOSFETs, and power supplies. Both the HFB and the DAHB are considered to use the same controller.

In the figure, \$4.2 per cell is the cost target of BMS + APM in EV OEMs as of 2020 [30]. Based on a survey of component pricing, the costs of the systems are extrapolated to mass production. A 'break-even' point occurs when 16,684 EVs are sold and the battery balancing approaches the free of charge point. Assuming both configurations use the same model of MOSFETs, the proposed configuration achieves up to a decrease of 22% in associated costs compared with a HFB thanks to the topological improvement and the core removal.

VI. Conclusions

This study proposes a drastically simplified DAHB topology for facilitating the adoption of redistributive balancing in EV applications. The cost improvement is achieved through topological and material reductions, i.e., fewer switches and a coreless transformer. The system model involving the coupling coefficient is analyzed to help make design choices, such as operating frequency and transformer characteristics. The expression of the output power is given to guarantee the

TABLE II: The primary parameters of the coreless transformer.

Magnetization inductance	Leakage inductance
141.5 nH	24.9 nH
coupling coefficient	**Effective turns ratio**
0.85	3.74

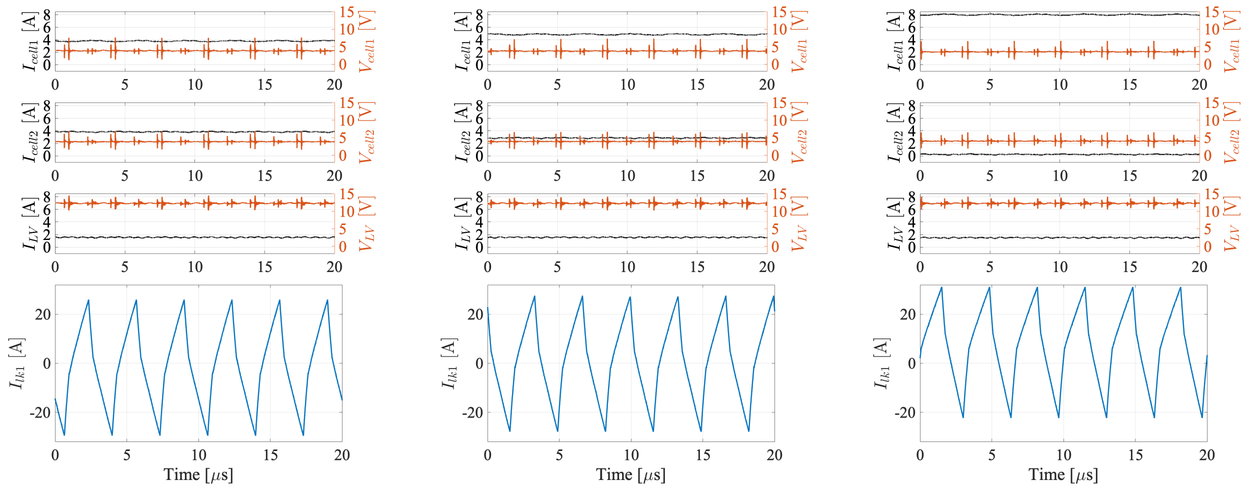

(a) (b) (c)

Fig. 12: The measured waveforms at 300 kHz when consuming 30 W with the conditions of (a) $I_{DC} = 0A, I_{cell1} = I_{cell2} = 3.8A$, (b) $I_{DC} = 2A, I_{cell1} = 4.8A, I_{cell2} = 2.8A$, (c) $I_{cell1} = 7.6A, I_{cell2} = 0A$ (replotted in MATLAB).

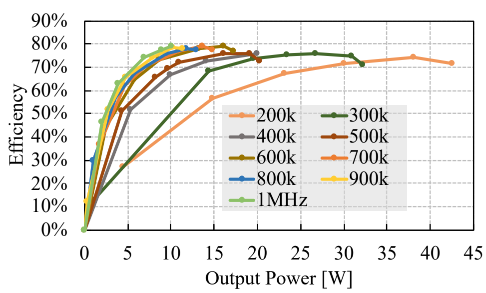

Fig. 13: The measured efficiency with respect to output power at different operating frequencies.

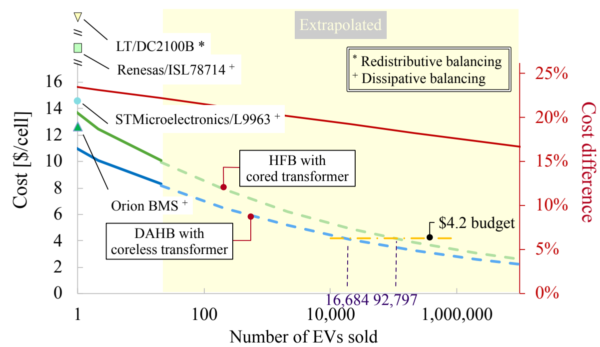

Fig. 14: The cost difference between an HFB with a core and a coreless DAHB.

rated power of the loosely coupled transformer. A prototype is developed and verified through the identified balancing modes, including C2LV and C2C. Therefore, the prototype is validated to provide all balancing modes while simplifying the construction of the BB-APM. The cost of the BB-APM system is lowered by 22% as compared to the HFB topology, allowing it to approach cost competitiveness with inefficient dissipative balancing.

The efficiency of the setup can be improved to approach other converters by implementing several changes including the use of discrete MOSFETs and/or more advanced switches such as GaN or SiC that have improved characteristics. Further, advanced control techniques such as variable frequency switching can be used to reduce switching losses. These limitations are compensated for by a reduction in the number and type of components and thus a decrease in overall costs.

References

[1] T. Baumhöfer *et al.*, "Production caused variation in capacity aging trend and correlation to initial cell performance," *Journal of Power Sources*, vol. 247, pp. 332–338, 2014.

TABLE III: Comparison among modular battery balancing topologies for a battery system with 2n cells

Topology (MOSFET technology)	Components*	Balancing modes	Balancing Speed	Efficiency	Required power level	Switching frequency
Proposed topology (Si)	$4n/0$	C2C + C2LV + LV2C	Fast $(< 1)^{+}$	80%	1.2 - 2.4 kW	100k Hz - 1 MHz
HFB (GaN) [2]	$6n/n$	C2C + C2LV + LV2C	Fast $(< 1)^{+}$	89.1%	1.2 - 2.4 kW	1 MHz
DAB (Si) [28]	$16n/2n$	C2LV + LV2C	Relatively fast $(< 1)^{+}$	92%	1.2 - 2.4 kW	200kHz
Inductive (N/A) [12]	$2n/2n$	C2C	Slow $(> 20)^{+}$	86%	0.5 - 2 KW	100kHz
Buck-boost (Si) [15]	$4n/2n$	C2HV+ HV2C	Relatively fast $(< 1)^{+}$	93%	60 - 380 kW (HV bus)	250kHz

*Number of power switches/ferromagnetic cores

+Number of hours to balance for a 100-cell pack under same condition [29]

[2] W. Wang and M. Preindl, "Dual Cell Links for Battery-Balancing Auxiliary Power Modules: A Cost-Effective Increase of Accessible Pack Capacity," *IEEE Transactions on Industry Applications*, vol. 56, no. 2, pp. 1752–1765, 2020.

[3] J. Cao, N. Schofield, and A. Emadi, "Battery balancing methods: A comprehensive review," in *Vehicle Power and Propulsion Conference*, 2008.

[4] S. W. Moore and P. J. Schneider, "A Review of Cell Equalization Methods for Lithium Ion and Lithium Polymer Battery Systems," in *SAE World Congress*, 2001.

[5] M. Daowd *et al.*, "Passive and active battery balancing comparison based on MATLAB simulation," *IEEE Vehicle Power and Propulsion Conference*, 2011.

[6] K. G.A., "Switched-capacitor systems," in *Modern Technique and Technologies*, 2000, pp. 57–59.

[7] C. Pascual and P. Krein, "Switched capacitor system for automatic series battery equalization," *Applied Power Electronics Conference*, 1997.

[8] N. H. Kutkut *et al.*, "Design considerations for charge equalization of an electric vehicle battery system," *IEEE Transactions on Industry Applications*, vol. 35, no. 1, pp. 28–35, 1999.

[9] S. Li, C. C. Mi, and M. Zhang, "A high-efficiency active battery-balancing circuit using multiwinding transformer," *IEEE Transactions on Industry Applications*, vol. 49, no. 1, pp. 198–207, 2013.

[10] T. Bui *et al.*, "A Modular Cell Balancer Based on Multi-Winding Transformer and Switched-Capacitor Circuits for a Series-Connected Battery String in Electric Vehicles," *Applied Sciences*, vol. 8, Aug. 2018.

[11] M. Evzelman *et al.*, "Active Balancing System for Electric Vehicles With Incorporated Low-Voltage Bus," in *IEEE Applied Power Electronics Conference and Exposition*, 2014, pp. 3230–3236.

[12] P. A. Cassani and S. S. Williamson, "Design, testing, and validation of a simplified control scheme for a novel plug-in hybrid electric vehicle battery cell equalizer," *IEEE Transactions on Industrial Electronics*, vol. 57, no. 12, pp. 3956–3962, 2010.

[13] C. S. Moo, K. S. Ng, and Y. C. Hsieh, "Parallel operation of battery power modules," *IEEE Transactions on Energy Conversion*, vol. 23, no. 2, pp. 701–707, 2008.

[14] M. Einhorn *et al.*, "A current equalization method for serially connected battery cells using a single power converter for each cell," *IEEE Transactions on Vehicular Technology*, vol. 60, no. 9, pp. 4227–4237, 2011.

[15] Y. Li and Y. Han, "A Module-Integrated Distributed Battery Energy Storage and Management System," *IEEE Transactions on Power Electronics*, no. 99, 2016.

[16] M. Preindl, "A Battery Balancing Auxiliary Power Module with Predictive Control for Electrified Transportation," *IEEE Transactions on Industrial Electronics*, vol. 0046, no. c, pp. 1–1, 2017.

[17] N. Ghaeminezhad *et al.*, "Active cell equalization topologies analysis for battery packs: A systematic review," *IEEE Transactions on Power Electronics*, vol. 36, no. 8, pp. 9119–9135, 2021.

[18] H. Zhang *et al.*, "Active battery equalization method based on redundant battery for electric vehicles," *IEEE Transactions on Vehicular Technology*, vol. 68, no. 8, pp. 7531–7543, Aug. 2019.

[19] F. Z. Peng *et al.*, "A new ZVS bidirectional DC-DC converter for fuel cell and battery application," *IEEE Transactions on Power Electronics*, vol. 19, no. 1, pp. 54–65, 2004.

[20] K. Zhang, Z. Shan, and J. Jatskevich, "Large- and Small-Signal Average-Value Modeling of Dual-Active-Bridge DC–DC Converter Considering Power Losses," *IEEE Transactions on Power Electronics*, vol. 32, no. 3, pp. 1964–1974, Mar. 2017.

[21] F. Krismer and J. W. Kolar, "Accurate power loss model derivation of a high-current dual active bridge converter for an automotive application," *IEEE Transactions on Industrial Electronics*, vol. 57, pp. 881–891, 2010.

[22] S. Y. Hui, S. C. Tang, and H. S. H. Chung, "Some electromagnetic aspects of coreless PCB transformers," *IEEE Transactions on Power Electronics*, vol. 15, no. 4, pp. 805–810, 2000.

[23] W. Wang and M. Preindl, "Maximum-power-per-ampere variable frequency modulation for dual active bridge converters in battery balancing application," *IEEE Transactions on Industrial Electronics*, vol. 69, pp. 5900–5909, 2022.

[24] E. Brenner and M. Javid, *Analysis of Electric Circuits*. McGraw-Hill, 1959.

[25] H. Li, F. Z. Peng, and J. S. Lawler, "A natural ZVS medium-power bidirectional DC-DC converter with minimum number of devices," *IEEE Transactions on Industry Applications*, vol. 39, no. 2, pp. 525–535, 2003.

[26] A. Rodríguez *et al.*, "Different purpose design strategies and techniques to improve the performance of a dual active bridge with phase-shift control," *IEEE Transactions on Power Electronics*, vol. 30, pp. 790–804, 2015.

[27] R. Hou and A. Emadi, "Evaluation of Integrated Active Filter Auxiliary Power Modules in Electrified Vehicle Applications," Thesis, McMaster University, 2015, p. 217.

[28] D. Costinett *et al.*, "Active balancing system for electric vehicles with incorporated low voltage bus," in *2014 IEEE Applied Power Electronics Conference and Exposition - APEC 2014*, 2014.

[29] M. Preindl, C. Danielson, and F. Borrelli, "Performance evaluation of battery balancing hardware," in *European Control Conference (ECC)*, 2013, pp. 4065–4070.

[30] UBS Evidence Lab, "Electric Car Teardown – Disruption Ahead?" Tech. Rep. May, 2017, p. 95.